Version of Record: https://www.sciencedirect.com/science/article/pii/S002231151930282X
Manuscript_7241e46f1869dc5b82078319e3873a19

Damage Mechanics Modeling of the Non-linear Behavior of SiC/SiC Ceramic Matrix Composite Fuel Cladding

Mohammad Alabdullah and Nasr M. Ghoniem

Department of Mechanical & Aerospace Engineering, University of California, Los Angeles (UCLA), 420 Westwood Plaza, Los Angeles, CA. 90095-1597, U.S.A.

Abstract

A damage model is developed and validated with experimental data for the non-linear mechanical behavior of SiC/SiC composite materials in nuclear applications. The model extends a continuum damage mechanics formalism, where explicit property degradation and volumetric swelling as a result of neutron irradiation are additionally included. The model is shown to be validated with out-of-pile experiments, and then applied to off-normal and high-burnup operating conditions associated with loss of cooling and extended radiation exposure, respectively. Optimized operating conditions aimed at reducing the fuel temperature included variation of the thermal conductivity and initial fuel-cladding gap thermal resistance. The nonlinear response along with continuum micro-cracking damage predictions are obtained and compared to the behavior during normal operating conditions. Numerical implementation of the model is based on 3-D Finite Element solutions.

Keywords: SiC/SiC composites, radiation damage, non-linear, fuel cladding, high-temperature.

*To whom correspondence should be addressed;
Email: malanzey88@gmail.com

Contents

1. Introduction

High-temperature composite materials have broad applications in the energy sector due to their unique capabilities to sustain strength at elevated temperatures, inert interaction with most coolants, and their high strength-to-weight ratio. These encompass SiC/SiC composites, developed for nuclear applications as fuel cladding in light water reactors (LWR). In addition to the excellent thermo-mechanical properties of SiC, the material exhibits high irradiation resistance, especially in the crystalline high purity and stoichiometric form (e.g. the chemically vapor deposited SiC (CVD) material [1]). During the early stages of SiC/SiC CMC development, ceramic grade Nicalon fibers were not stable under neutron irradiation. However fibers with high crystallinity and purity (e.g. Nicalon Type-S and Tyranno SA), could be manufactured and were found to be more stable under irradiation [2]). This development has opened the door to further advance SiC/SiC composites for nuclear applications, where significant research has been conducted to characterize their properties[3].

Due to recent advances in composite fabrication, SiC/SiC CMC is becoming a very strong candidate to replace Zr-based fuel cladding in water reactors. Ever Since the Fukushima Daiichi nuclear plant accident, significant research efforts have been dedicated to develop accident tolerant fuel cladding systems, focusing primarily on oxidation resistance. The accident took place due to loss of cooling (LOCA) as a result of the tsunami following an earthquake. Loss of cooling resulted in an increase in cladding temperature, which led to an oxidation chemical reaction between the cladding material and the high temperature steam releasing explosive hydrogen gas that eventually caused an explosion. SiC/SiC composite materials with their exceptional resistance to steam oxidation and neutron irradiation [4] have emerged as attractive materials to replace zircaloy cladding in order to achieve an accident-tolerant system. It is noted that SiC/SiC CMC cladding can still generate substantial amounts of hydrogen, its use in design helps delay the consequences of LOCA accidents, but not eliminate their consequences[5].

A number of studies have been conducted to examine the thermo-mechanical behavior of SiC/SiC fuel cladding under neutron irradiation. Carpenter et. al examined the behavior of a SiC/SiC CMC cladding in pressurized water reactors using a modified FRAPCON fuel performance code [6]. More recently, Ben-Belgacem et. al [7], and Singh et. al developed a framework for the thermo-mechanical analysis of the in-pile performance of SiC/SiC composite fuel cladding in LWRs and PWRs [2, 8]. In the conceptual design investigation of Lan et. al [9], multi-layered SiC/SiC cladding was modeled, where the stress distribution of a triple-layered SiC/SiC CMC was obtained.

Recent work from the MIT group [10] and the GA group [11] developed models that capture the behavior of SiC/SiC composites at higher stresses. Failure probabilities of a single pin (Stone) and full core (Deng) due to cold shutdown were introduced. In addition, pellet-cladding mechanical interaction, which leads to stresses exceeding the matrix cracking stress for a multilayer cladding was analyzed. In these two models, the stress/strain non-linearity due to CMC micro-cracking was included through pseudo plastic models. Here, one needs to define the matrix cracking stress and the corresponding strain where the elastic modulus changes as a function of the stress/strain history[10] of the composite. Moreover, off-normal operating conditions due to loss of coolant accident (LOCA) was also investigated by Wagih et al. [12] and by Avincola et al.[13], where a pseudo plastic model based on modified stress strain curves were used to capture the non-linear behavior of the CMC. In this work, the theory of thermo-elasticity was utilized to include radial temperature gradients and radiation-induced swelling. These models

added to our current understanding of the influence on the mechanical state of changes in the properties of SiC/SiC composites under variable temperature and irradiation dose. Although these models have opened the door to design and predict the mechanical behavior of SiC/SiC cladding, a self-consistent damage evolution and non-linear deformation at high stress and neutron irradiation is still lacking.

In the present work, we develop a continuum thermodynamic damage model, where the non-linear response due to matrix micro-cracking generated under high multiaxial thermo-mechanical loading is described. Such behavior is critically important in severe environments, where off-normal operating conditions similar to those contributed into the hydrogen explosion of Fukushima Diiachi nuclear plant are expected. Under these conditions, the theory of elasticity is insufficient to capture the materials response. Moreover, SiC-based cladding has made it possible to design higher performance fuels that have mechanical integrity at high burnup. Micro-cracking of the composite is expected at high burnups due to increased release of fission gases in the gap between the fuel pellet and the inner cladding surface. This, in turn, results in higher internal pressure [6, 8] and hence the non-linear mechanical response. Although previously developed models of SiC/SiC cladding have shed considerable light on the effects of high temperature and irradiation on the mechanical response, they are limited in their predictions of the post-elastic response under multi-axial loading conditions. The mechanical state of the fuel cladding during off-normal or extended operating conditions needs to be fully described in a self-consistent manner with micro-cracking damage evolution. Unlike conventional Zircaloy fuel cladding, SiC/SiC CMCs include natural defects (namely micro-cracks), and additional micro-cracks are generated as the material is subjected to neutron irradiation. Beyond the micro-cracking stress limit (analogues to yield stress in metals), the density of micro-cracks increases as tensile stresses increase until failure occurs at a strain that is generally 7 times larger than the micro-cracking strain limit. This observation might allow us to design beyond the micro-cracking stress limit in order to obtain a more efficient fuel cladding system, where limited micro-cracking is tolerated before catastrophic failure. The main objective here is to extend previously established damage models (pioneered for Aerospace applications) to nuclear applications by explicitly accounting for property degradation, thermal expansion effects, as well as volumetric swelling due to neutron irradiation. The present model has some unique features that would hopefully extend the range of applicability of earlier efforts. These are listed below:

1. It accounts for the non-linearity in the stress-strain behavior using a continuum thermodynamic damage approach, by linking damage evolution parameters to the instantaneously reduced stiffness matrix in a multiaxial framework.
2. It captures the non-linearity due to multiaxial loading imposed by coupled hoop and axial stresses, where damage in the hoop direction precedes that in the axial direction.
3. It describes multiaxial unloading behavior, where the slope of the stress-strain curve upon unloading changes due to accumulated damage. Thus, the model has the capacity to simulate cyclic loading and unloading operations, accounting for gradual damage accumulation and stiffness degradation.
4. The spatial distribution of the magnitude of microcracking damage (micro-crack density) can be determined, and potentially used in failure theories in future follow-up studies. Operational regimes where the damage spreads across the entire cross-section can therefore be identified.

In Section 2, we summarize the continuum damage mechanics model, where we introduce relevant damage variables and their relationship to SiC/SiC architecture and to the stiffness matrix of the composite. Since the damage model is phenomenological, it contains a number of parameters that can be extracted from experimental observations. Model calibration with available properties is discussed in the same section, then applied to predict multiaxial behavior and compare to experimental data. The multiphysics framework that encompasses the damage model, together with elements of thermomechanics is also presented in Section 2. Applications of the model then follows, first by defining typical reactor operational scenarios under both normal and off-normal conditions in Section 3. Results of the multiphysics model for the simulation of the effects of normal and off-normal operational conditions on the cladding mechanical behavior are given in Section 4. Some of the input parameters to these simulations are not well-known to a precise degree, and hence a sensitivity analysis of the impact of parameter uncertainties is given in Section 5. Finally, conclusions of this work are summarized in Section 6.

2. Methodology

2.1. Thermo-mechanical Damage Model

Within the framework of continuum damage mechanics, the concept of a damage "field" is introduced to describe a distributed form of incompatibly, where the material in damaged zones cannot bear a mechanical force. Several types of physical manifestations have been associated with this phenomenological concept, such as voids, micro-cracks, debonded fibers, etc. [14]. In the case of CMCs, this concept implies a description of the density of sub-microscopic micro-cracks, for which a traditional fracture mechanics analysis would be impossible. Here, damage can be defined in terms of the area that does not support loads due to cracks and voids. If we take (dA) to be the total surface area of the material and (dA_D) to be the surface area of the damaged material (voids cracks), then we can express the area that carries the load as $dA_0 = dA - dA_D$ where dA_0 represents an effective area. Once the concept of the effective area is established, a damage variable can be defined as $D = \frac{dA_D}{dA}$, where $D = 0$ when the material is undamaged (pristine) and $D = 1$ when the material is completely damaged (fractured). Under a simple uniaxial loading, the effective area that carries the load $(\tilde{A})$ can be expressed in terms of the damage variable and the total surface area $d\tilde{A} = (1 - D)dA$. The effective stress of an *equivalent* undamaged bar, which has the same strain of the damaged condition can thus be written as $\tilde{\sigma} = \frac{dF}{d\tilde{A}} = \frac{\sigma}{1-D}$. Since the damage variable cannot be measured directly, one has to use a general principle to connect the mechanical state of the damaged material and the *equivalent* state. In the simplest case, one enforces the condition that the strain is the same in the two states, thus: $\epsilon = \frac{\sigma}{E(D)} = \frac{\tilde{\sigma}}{E_0}$, where the stiffness (elastic modulus), is a function of the damage variable in the damaged material, and is taken as the pristine stiffness in the equivalent undamaged material. This results in finding the *true* stress $\tilde{\sigma}$, as: $\tilde{\sigma} = \frac{E_0}{E(D)}\sigma$ where σ is the average stress and E_0 is the stiffness in the undamaged state. Damage can then be quantified by simply measuring the change in stiffness of the material (either by loading and unloading or thorough acoustic waves).

This brief and simple approach for uniaxial deformation aims at illustrating how damage is defined and introduced into the material. In order to extend this definition to encompass anisotropic materials such as SiC/SiC CMC, one has to extend the previous scalar representation to a tensorial formulation. Taking a damaged area in the material $(d\tilde{A})$ and defining a unit

normal ($\tilde{\boldsymbol{v}}$) vector to the damaged area, then one can show that the vector area $\boldsymbol{v}dA$ in the damaged material is linearly transformed to the vector area $\tilde{\mathbf{n}}d\tilde{A}$ in the *equivalent* material, as: $\tilde{\boldsymbol{v}}d\tilde{A} = (\boldsymbol{I} - \boldsymbol{D})\boldsymbol{v}dA$, where $\boldsymbol{D}$ is a second rank damage tensor consisting of damage scalar variables mapping the damaged stiffness to the pristine one [14]. The effective stress tensor $\tilde{\boldsymbol{\sigma}}$ can then be obtained from the average stress tensor $\boldsymbol{\sigma}$ as: $\tilde{\boldsymbol{\sigma}} = (\mathbf{I} - \mathbf{D})^{-1}\boldsymbol{\sigma}$. Since this form is generally not symmetric, the following rotation proposed by Cordebois and Sidoroff[15]) $\tilde{\boldsymbol{\sigma}}^S = [(\boldsymbol{I} - \boldsymbol{D})^{-1}\boldsymbol{\sigma} + \boldsymbol{\sigma}(\boldsymbol{I} - \boldsymbol{D})^{-1}]/2$ produces a symmetric equivalent stress tensor. If one finds the principal values D_i and directions $\boldsymbol{n}_i$ of the damage tensor, then it can be expressed in the spectral form: $\boldsymbol{D} = \sum_{i=1}^{3} D_i \boldsymbol{n}_i \otimes \boldsymbol{n}_i$. Therefore, the effective area in the equivalent state is expressed as: $d\tilde{A}_i = (1 - D_i)dA_i$, with no sum over i.

Now we represent the damage tensor as a linear sum of three independent tensors, each resulting from a specific form of damage. Traditionally, damage in CMCs is ascribed solely to mechanical strain, and the corresponding tensor is $\boldsymbol{D}^m$. We extend this further by adding damage due to irradiation-induced swelling: $\boldsymbol{D}^{irr}$, and another component due to thermal gradients across the thickness $\boldsymbol{D}^{\nabla T}$. The principal values D_i are the void and point defect area fraction intercepted by the principal planes of $\boldsymbol{D}$. Because neutron irradiation produces a spatially uniform distribution of voids and point defects at temperatures where vacancies are not readily mobile[16] in SiC/SiC, the principal values of $\boldsymbol{D}^{irr}$ will all be equal to $S^{2/3}$, where S is the volumetric swelling fraction that can be easily determined from experiments.It is worth mentioning that recent work by Katoh [17] has illustrated that irradiation swelling in SiC/SiC is in fact anisotropic. However, in this work the contribution of irradiation swelling to the damage tensor is taken as isotropic for the sake of simplicity. We conclude from this discussion that an irradiated material that is not mechanically or thermally loaded will accumulate damage as a function of fluence that renders it less stiff as the irradiation dose increases. In the following, we discuss additional mechanical and thermal damage contributions.

During the fuel cladding operation, several sources of strain will contribute to its deformation: elastic ($\boldsymbol{\epsilon}^e$), swelling ($\boldsymbol{\epsilon}^s$), and thermal ($\boldsymbol{\epsilon}^{th}$). In this work swelling will be treated as a function of temperature and irradiation dose. Because the temperature is not uniform in the SiC/SiC cladding, swelling will also be non-uniform, resulting in internal stresses, even in the absence of mechanical loads. Since SiC/SiC does not exhibit significant creep deformation at temperatures below 1200 °C, then its contribution to deformation strain will be ignore here. The total strain is given by:

$$\boldsymbol{\epsilon}^t = \boldsymbol{\epsilon}^e + \boldsymbol{\epsilon}^{th} + \boldsymbol{\epsilon}^s \tag{1}$$

We note here that the additional strain components due to swelling is dilatational and is simply given by $\boldsymbol{\epsilon}^s = \frac{1}{3}e\boldsymbol{I}$, where $\boldsymbol{I}$ is the identity matrix, and $e = \frac{\Delta V}{V}$ is the irradiation-induced volumetric swelling. Thus, the corresponding statement of the damage tensor is given by:

$$\boldsymbol{D}^t = \boldsymbol{D}^m + \boldsymbol{D}^{\nabla T} + \boldsymbol{D}^{irr} \tag{2}$$

$\boldsymbol{D}^t$ is the total damage tensor, which takes the following form (in Voigt notation)

$$\boldsymbol{D}^t = \begin{bmatrix} d_1^m + d_1^{\nabla T} + d_1^s & 0 & 0 & 0 & 0 & 0 \\ 0 & d_2^m + d_2^{\nabla T} + d_2^s & 0 & 0 & 0 & 0 \\ 0 & 0 & d_3^m + d_3^{\nabla T} + d_3^s & 0 & 0 & 0 \\ 0 & 0 & 0 & d_4^m & 0 & 0 \\ 0 & 0 & 0 & 0 & d_5^m & 0 \\ 0 & 0 & 0 & 0 & 0 & d_6^m \end{bmatrix} \tag{3}$$

where d_i^m , $d_i^{\nabla T}$, d_i^s are the scalar damage variables associated with mechanical loading, temperature gradient, and irradiation, respectively. It is worth mentioning that the damage tensor introduced in Eq (3) has a similar structure to that introduced by Chabouche and Maire [18] in their tensorial damage model. However, in this work, the damage tensor was extended to include contributions from temperature gradients and irradiation. Here, the damage tensor due to irradiation is expressed as an isotropic tensor, with equal components that represent the fractional area of any plane intercepting voids and helium bubbles resulting from neutron irradiation, that is $\boldsymbol{D}^{irr}$ with components $D_i^{irr} = e^{2/3}$, for $i = 1, 2, 3$.

The damage tensor resulting from temperature gradients alone will not be included here for simplicity, and future efforts are planned to explore its behavior. The model is further developed by obtaining the elastic strain (including damage contribution) from the total strain. On the other hand, the stress field can be readily computed from the elastic strain using a generalized Hooke's law with a damaged stiffness tensor.

$$\boldsymbol{\sigma} = \mathcal{S}^d : \boldsymbol{\epsilon}^e \tag{4}$$

where $\mathcal{S}^d$ is the damaged stiffness tensor. The damage model implemented in this analysis is the key to predict nonlinear behavior of the SiC-based cladding, since it impacts the stiffness tensor directly ($\mathcal{S}^d$), and hence shows nonlinearity beyond the matrix cracking threshold stress.

A continuum damage model has been formulated within the framework of equilibrium thermodynamics capturing the non-linear behavior of the SiC/SiC CMC. The 2-D mechanical damage model will be based on the assumption of plane stress, which is valid in the case of a fuel cladding (thin wall tube), where only in-plane damage is taken into consideration. The proposed model uses variables that describe damage in a laminate composites [14] to model damage evolution in CMCs. A good example for this approach is the C/SiC CMC model proposed by Li [19]. For the fuel cladding, through-the-thickness stress (radial) is negligible, and to a good approximation, we can proceed with a 2-D plane stress implementation of the model. By taking the coordinate system shown in the Figure(1) to be the material's local coordinate system while assuming $0/90$ layup with the fibers parallel and perpendicular to the axial direction. Furthermore, we use the Voigt notation for the stress and strain tensors, as: $[\sigma_p] = [\sigma_{11}\ \sigma_{22}\ \sigma_{33}\ \sigma_{23}\ \sigma_{13}\ \sigma_{12}]^T = [\sigma_1\ \sigma_2\ \sigma_3\ \sigma_4\ \sigma_5\ \sigma_6]^T$, and similarly for strain $[\gamma_q]$. $[\sigma_p]$ is a column stress vector. Thus, $[\sigma_p] = [S_{pq}][\gamma_q]$, or $\sigma_p = S_{pq}\gamma_q$, where $[S_{pq}]$ is a 6×6 stiffness matrix. The elastic energy density is $W = \frac{1}{2} S_{pq}\gamma_p\sigma_q$, with summation from $p\&q = 1...6$. The corresponding compliance matrix is $[C_{pq}]$. For the case of laminated SiC/SiC, with laminate plane normals along the **1**-direction (radial), the material is orthotropic with 9 independent elastic constants instead of 36. If fibers are wound at $0/90$, it becomes transversely isotropic with only 5 elastic constants. For the cladding material, the material is generally orthotropic with

the following compliance and elastic constants: $C_{11} = \frac{1}{E_1}$; $C_{22} = \frac{1}{E_2}$; $C_{33} = \frac{1}{E_3}$; $C_{12} = -\frac{\nu_{12}}{E_1}$; $C_{23} = -\frac{\nu_{23}}{E_2}$; $C_{13} = -\frac{\nu_{13}}{E_3}$; $C_{44} = \frac{1}{G_{23}}$; $C_{55} = \frac{1}{G_{13}}$; $C_{66} = \frac{1}{G_{12}}$. Furthermore, the stress system under plane stress assumption is 2-dimensional, and the only relevant components are then σ_2, σ_3 and σ_4 (in-plane shear) for the mechanical damage, significantly simplifying the analysis.

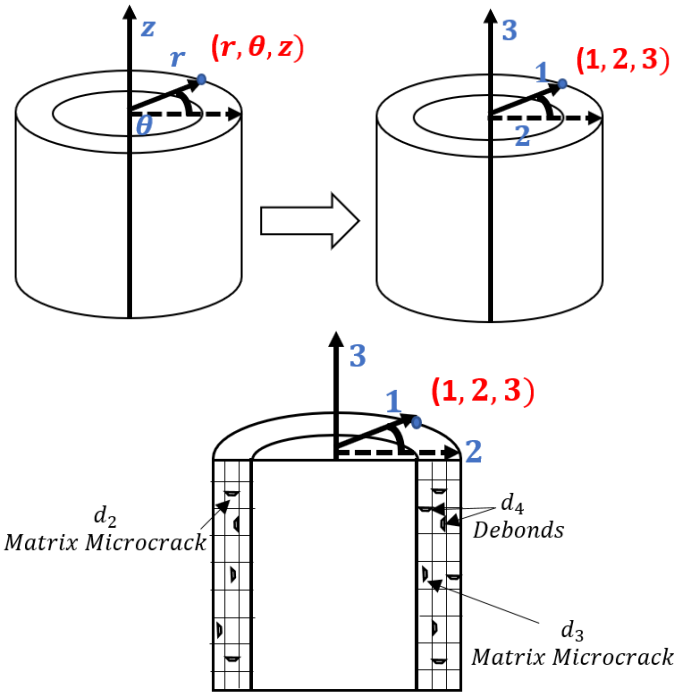

Figure 1: Material local coordinate system (MLCS) and scalar damage variables represented along with the composites architecture

Damage can be introduced into the SiC/SiC fuel cladding system by defining the true stresses and the associated damage variables with relevant components as: $\tilde{\sigma_1}$, $\tilde{\sigma_2}$, $\tilde{\sigma_3}$, $\tilde{\sigma_4}$ and corresponding damage variables: d_1^t, d_2^t, d_3^t, d_4^t respectively, where

$$\begin{cases} d_i^t = d_i^m + d_i^s & \text{for } i = 1, 2, 3 \\ d_i^t = d_i^m & \text{for } i = 4 \end{cases} \tag{5}$$

Note that the mechanical damage is associated with the in-plane true stress components, while the irradiation damage influences the diagonal components of the stress tensor since bubble and void eignestrains are isotropic. The presented mechanical damage scalar variables are also related to the composites architecture as shown in Figure (1), where the damage variables d_2^m, $d_3^m$and d_4^m are associated with the degradation of the elastic moduli E_2 and E_3, along with the degradation of the in-plane shear modulus G_{23}. The d_2^m and d_3^m damage variables express the magnitude of matrix micro-cracking in the orthogonal fiber directions 2 and 3, as shown in Figure(1) due to mechanical forces alone. This assumption is based on the experimental observations that elastic brittle damage for CMCs is developed such that cracks are either parallel or perpendicular to fiber orientations, while the d_4^m damage scalar variable quantifies the amount of matrix-fiber debonding [14, 20]. By taking the coordinate system shown in Figure (1) to be

the material's local coordinate system while assuming $0/90$ layup with the fibers parallel and perpendicular to the axes, the associated damage scalar variables are:

$$d_1^t = 1 - \frac{E_1}{E_1^0}; \quad d_2^t = 1 - \frac{E_2}{E_2^0}; \quad d_3^t = 1 - \frac{E_3}{E_3^0}; \quad d_4^t = 1 - \frac{G_{23}}{G_{23}^0} \tag{6}$$

where E_1,E_1^0, E_2,E_2^0 and E_3,E_3^0 are the damaged and initial elastic moduli in the hoop and axial directions, respectively, while G_{23}, G_{23}^0 are the damaged and initial in-plane shear moduli, respectively, for the SiC-cladding. The damaged moduli can be obtained from a combination of the unloading slope in cyclic tensile loading/unloading tests and from the fact that $d_i^s = e^{2/3}$ for $i = 1, 2, 3$.

The Gibbs free energy is introduced here as a function of deformation (stress), temperature, and internal variables (in this case, the damage variables, the temperature gradient, and the irradiation-induced dilatation (swelling)). Extending the standard Gibb's energy per unit mass of a stressed 2-D composite [14], Γ^{te}, we then have,

$$\begin{aligned} -\rho\Gamma^{te}(\sigma_i, d_i, T, e) = \frac{1}{2}\Bigg[& \frac{<\sigma_1>^2}{E_1^0(1-d_1^t)} + \frac{<\sigma_2>^2}{E_2^0(1-d_2^t)} + \frac{<\sigma_3>^2}{E_3^0(1-d_3^t)} + \frac{\sigma_4^2}{G_{23}^0(1-d_4^t)} \\ & + \frac{\sigma_5^2}{G_{13}^0} + \frac{\sigma_6^2}{G_{12}^0} - \left(\frac{\nu_{12}^0}{E_1^0} + \frac{\nu_{21}^0}{E_2^0}\right)\sigma_1\sigma_2 - \left(\frac{\nu_{13}^0}{E_1^0} + \frac{\nu_{31}^0}{E_3^0}\right)\sigma_1\sigma_3 - \left(\frac{\nu_{23}^0}{E_2^0}\right. \\ & \left. + \frac{\nu_{32}^0}{E_3^0}\right)\sigma_2\sigma_3 + 2(T - T_0)(\alpha_{11}\sigma_1 + \alpha_{22}\sigma_2 + \alpha_{33}\sigma_3) + \frac{2e}{3}tr(\boldsymbol{\sigma})\Bigg] \end{aligned} \tag{7}$$

ρ is the density,α_{ij} are the thermal expansion coefficients along the material's orthotropic axis, T, T_0 are the current and reference temperatures, respectively, σ_i, for $i \in [1, 6]$, are the components of the Cauchy stress tensor $\boldsymbol{\sigma}$ in Voigt notation, and ν_{ij}^0 are the Poisson's ratios of the undamaged material. Damage variables in the energy equation Eq (7) are not introduced in the Poisson's terms, because experimental observations indicate that matrix micro-cracking occurs perpendicular to the loading direction [21], leaving the compliance matrix off-diagonal terms unchanged. The first two lines on the right hand side of Eq. 7 represent the stored elastic energy per unit volume due to the mechanical stress, while the last line gives the contributions of thermal and volumetric expansion to the work done against the applied mechanical stress. Here, we use the notation $<x>= 0$ if $x < 0$ to guarantee micro-crack closure for compressive stresses. It is worth mentioning that irradiation swelling has a progressive damaging effect on the mechanical properties [2]. This degradation, which will be discussed in detail on section 2.3, will be introduced as an additional damage component that results in a decrease in the stiffness matrix due to radiation-induced volumetric strain.

The Gibbs free energy is used to determine model parameters by taking appropriate variational derivatives. The total strain field is $\boldsymbol{\epsilon}^t = -\rho\frac{\partial\Gamma}{\partial\boldsymbol{\sigma}}$, which according to Eq. 1 is detailed as:

$$\boldsymbol{\epsilon}^t = \mathcal{C}^d : \boldsymbol{\sigma} + \boldsymbol{\alpha}(T - T_0) + \frac{e}{3}\boldsymbol{I} \tag{8}$$

where $\mathcal{C}^d$ and $\boldsymbol{\alpha}$ are the compliance matrix of the damaged material and coefficient of thermal expansion tensor, respectively. On the other hand $\frac{e}{3}\boldsymbol{I}$ denotes the volumetric swelling dilatational strain, which is a function of both temperature and neutron fluence. The damaged mate-

rial's compliance matrix can be obtained from Gibb's energy by $\mathcal{C}^d_{ijkl} = -\rho \frac{\partial \Gamma}{\partial \sigma_{ij} \partial \sigma_{kl}}$, resulting in the matrix (in Voigt notation)[14]:

$$\mathcal{C}^d = \begin{bmatrix} \frac{1}{E_1^0(1-d_1^t)} & -\frac{\nu_{21}^0}{E_2^0} & -\frac{\nu_{31}^0}{E_3^0} & 0 & 0 & 0 \\ -\frac{\nu_{12}^0}{E_1^0} & \frac{1}{E_2^0(1-d_2^t)} & -\frac{\nu_{32}^0}{E_3^0} & 0 & 0 & 0 \\ -\frac{\nu_{13}^0}{E_1^0} & -\frac{\nu_{23}^0}{E_2^0} & \frac{1}{E_3^0(1-d_3^t)} & 0 & 0 & 0 \\ 0 & 0 & 0 & \frac{1}{2G_{23}^0(1-d_4^t)} & 0 & 0 \\ 0 & 0 & 0 & 0 & \frac{1}{2G_{13}^0} & 0 \\ 0 & 0 & 0 & 0 & 0 & \frac{1}{2G_{12}^0} \end{bmatrix} \tag{9}$$

From symmetry $\frac{\nu_{ij}^0}{E_i^0} = \frac{\nu_{ji}^0}{E_j^0};\ i\&j = 1, 2, 3$. The stress tensor can be numerically obtained from the strains by using the inverse of the compliance matrix (i.e. the stiffness tensor $\mathcal{S}^d$ of the damaged material.)

$$\boldsymbol{\sigma} = \mathcal{S}^d : \boldsymbol{\epsilon}^e = \mathcal{S}^d : \left(\epsilon^t - \boldsymbol{\alpha}(T - T_0) - \frac{e}{3}\boldsymbol{I} \right) \tag{10}$$

where $\boldsymbol{\epsilon}^e$ is the elastic strain tensor, and $\mathcal{S}^d$ is determined by inverting the compliance matrix $\mathcal{C}^d$.

$$\mathcal{S}^d = \begin{bmatrix} \frac{1-\nu_{32}^0\nu_{23}^0 {d'_1}^t}{E_2E_3\triangle} & \frac{\nu_{31}^0\nu_{23}^0(1-d_3^t)+\nu_{21}^0}{E_2^0E_3\triangle} & \frac{\nu_{21}^0\nu_{32}^0(1-d_2^t)+\nu_{31}^0}{E_2E_3^0\triangle} & 0 & 0 & 0 \\ \frac{\nu_{13}^0\nu_{32}^0(1-d_3^t)+\nu_{12}^0}{E_1^0E_3\triangle} & \frac{1-\nu_{13}^0\nu_{31}^0 {d'_2}^t}{E_1E_3\triangle} & \frac{\nu_{31}^0\nu_{12}^0(1-d_1^t)+\nu_{32}^0}{E_1E_3^0\triangle} & 0 & 0 & 0 \\ \frac{\nu_{12}^0\nu_{23}^0(1-d_2^t)+\nu_{13}^0}{E_1^0E_2\triangle} & \frac{\nu_{13}^0\nu_{21}^0(1-d_1^t)+\nu_{23}^0}{E_1E_2^0\triangle} & \frac{1-\nu_{12}^0\nu_{21}^0 {d'_3}^t}{E_2E_3\triangle} & 0 & 0 & 0 \\ 0 & 0 & 0 & 2G_{23} & 0 & 0 \\ 0 & 0 & 0 & 0 & 2G_{13}^0 & 0 \\ 0 & 0 & 0 & 0 & 0 & 2G_{12}^0 \end{bmatrix} \tag{11}$$

where $\triangle = \frac{1-\nu_{23}^0\nu_{32}^0 {d'_1}^t - \nu_{13}^0\nu_{31}^0 {d'_2}^t - \nu_{12}^0\nu_{21}^0 {d'_3}^t - 2\nu_{12}^0\nu_{23}^0\nu_{31}^0 {d'_1}^t(1-d_1^t)}{E_1E_2E_3}$, ${d'_1}^t = (1-d_2^t)(1-d_3^t)$, ${d'_1}^t = (1-d_1^t)(1-d_3^t)$ and ${d'_3}^t = (1-d_1^t)(1-d_2^t)$. After introducing the damaged stiffness matrix, one can calculate the true stress based on the strain equivalance principle [14] using Eq (10).

$$\tilde{\boldsymbol{\sigma}} = \mathcal{S}^0 : (\boldsymbol{\epsilon}^t - \boldsymbol{\alpha}(T - T_0) - \frac{e}{3}\boldsymbol{I}) \tag{12}$$

where $\mathcal{S}^0$ is the stiffness matrix of the intact material. In order to map the true stress $\tilde{\boldsymbol{\sigma}}$ to the nominal stress $\boldsymbol{\sigma}$, we can substitute Eq (8) into (12), which will result in

$$\begin{aligned} &\tilde{\boldsymbol{\sigma}} = \mathcal{S}^0 : \mathcal{C}^d : \boldsymbol{\sigma} \approx (\boldsymbol{I} - \boldsymbol{D}^t)^{-1} : \boldsymbol{\sigma} \\ &(\boldsymbol{I} - \boldsymbol{D}^t)^{-1} \approx \mathcal{S}^0 : \mathcal{C}^d \end{aligned} \tag{13}$$

Practically, Eq (13) is applied for the sake of simplicity, while several developed models use Eq(13) as a valid approximation [19]. The Tensor $\boldsymbol{D}^t$ is generally not symmetric and can be solved for by applying the transformation discussed earlier: $\boldsymbol{D}^t = [\mathcal{S}^0 : \mathcal{C}^d + \mathcal{C}^d : \mathcal{S}^0]/2$, which

approximately gives the damage tensor proposed in Eq (3). Relevant values of the components of the undamaged stiffness tensor for SiC/SiC are given in Table 1. The thermodynamic forces

Table 1: Pristine (undamged) SiC/SiC CVI fuel cladding elastic properties [2]

Parameter	Units	Value
E_1^0	GPa	280
E_2^0	GPa	204
ν_{12}^0	N/A	0.16
ν_{32}^0	N/A	0.13
ν_{13}^0	N/A	0.16
G_{12}^0	MPa	198
G_{13}^0	MPa	198
G_{23}^0	GPa	90.3

that drive mechanical damage growth, which are defined as the energy release rates associated with *mechanical* damage production, are also obtained from the Gibb's free energy by taking variational derivatives with respect to the mechanical damage parameters:

$$\begin{cases} Y_2 = \rho \frac{\partial \Gamma}{\partial d_2^m} = \frac{1}{2E_2^0}\left[\frac{<\sigma_2>^2}{(1-d_2^t)^2}\right] \\ Y_3 = \rho \frac{\partial \Gamma}{\partial d_3^m} = \frac{1}{2E_3^0}\left[\frac{<\sigma_3>^2}{(1-d_3^t)^2}\right] \\ Y_4 = \rho \frac{\partial \Gamma}{\partial d_4^m} = \frac{1}{2G_{23}^0}\frac{\sigma_4^2}{(1-d_4^t)^2} = \frac{\tilde{\sigma}_4^2}{2G_{23}^0} \end{cases} \tag{14}$$

where Y_2 is the volumetric energy released in the hoop direction due to the production of damage d_2 as a result of matrix micro-cracking with crack faces aligned perpendicular to the hoop direction. Similarly for Y_3 in the axial direction, and for Y_4, which accounts for fiber-matrix debond cracks. Assuming that the thermodynamic forces associated with compression stresses do not contribute to damage evolution, one can only consider the above thermodynamic forces associated with tensile and shear stresses. Note that thermodynamic forces associated with irradiation damage variables are obtained directly from the relation: $d_i^s = e^{2/3}$ for $i = 1, 2, 3$. Since neutron irradiation induced swelling is generally small in SiC/SiC composites (a few percent), the irradiation damage contribution to damage is relatively small when compared to mechanically-indued micro-cracking. For the proposed model to be thermodynamically consistent, Clausius-Duhem's inequality of the second law, which accounts for positive entropy dissipation, has to be satisfied. Since damage is one of the dissipative phenomena, its kinetic law should automatically obey the conditions $\dot{d}_{i=2,3,4} \geq 0$. The observed difference of damage modes induced by tensile and shear loading, along with the positive dissipation conditions motivate postulation of multiple damage criteria for each damage scalar variable based on the simplifying assumption of a time independent process, where the dissipation potential is replaced by damage functions describing the surface limiting the undamaged domain [22]. This step is a direct extension of the Von Mises hypothesis that describes the yield surface and its subsequent evolution due to strain hardening in a ductile material loaded under multi-axial conditions. Taking into consideration the initial in-plane symmetry, which imposes an equivalence of this criterion in the **2**- and **3**-directions (θ& z-directions respectively) will give the following

general damage evolution conditions for the *damage surface* beyond the elastic micro-cracking thresholds:

$$\begin{cases} d_2 = f_2(< Y^*_{2,max} - Y_{02} >) \\ d_3 = f_2(< Y^*_{3,max} - Y_{02} >) \\ d_4 = f_4(< Y^*_{4,max} - Y_{04} >) \end{cases} \tag{15}$$

where $Y_{i,max}$ and Y_{0i} are the maximum effective thermodynamic forces throughout the loading history, and damage threshold values (corresponding to the onset of micro-cracking), respectively. Damage conjugate forces express the damage strain energy release rates due to stresses applied in directions corresponding to the local material coordinate system, where for example Y_2 is a function of stresses applied in the **2**-direction. In the case of a biaxial load or a load that is not aligned with the material coordinate system, coupling between the damage conjugate forces will emerge causing a significant impact on the damage evolution law. It is then necessary to introduce $Y^*_{i=2,3,4}$ scalar functions of thermodynamic forces $Y_{i=2,3,4}$, which delineate damage surfaces, including multiaxial coupling effects. The positive dissipation along with the assumption that the damage laws are derived from a multi-surface potential (proposed by Matzenmiller [23]) require scalar functions $f_{i=2,3,4}$ to be positive and the damage surface to be at least star convex with respect to the origin and positive [23]. The effective thermodynamic forces can then be introduced as.

$$\begin{cases} Y^*_2 = Y_2 + g_{24}(Y_4)Y_4 H(\tilde{\sigma}_2 + \tilde{\sigma}_3) \\ Y^*_3 = Y_3 + g_{34}(Y_4)Y_4 H(\tilde{\sigma}_2 + \tilde{\sigma}_3) \\ Y^*_4 = Y_4 + g_{42}(Y_2)Y_2 + g_{43}(Y_3)Y_3 \end{cases} \tag{16}$$

where $g_{24} = g_{34}$, and $g_{42} = g_{43}$ are monotonically-increasing functions representing damage coupling effects and obeying material symmetry. The factor $H(\tilde{\sigma}_2 + \tilde{\sigma}_3)$ is introduced in order to eliminate damage effects that may arise due to shear stresses through the coupling function g_{24} under combined compression and shear loads, where $H(X)$ is a Heaviside step-function. By incorporating the effective thermodynamic forces into the model, one can obtain damage evolution laws for the scalar variables as:

$$d_i = f_i(< Y^*_{i,max} - Y_{0i} >) = a_i - \frac{a_i}{1 + (\frac{Y_{i,max} - Y_{0i}}{b_i})^{c_i}} \quad (i = 2, 4) \tag{17}$$

where a_i, b_i and c_i are damage upper limits (saturation), normalizing thermodynamic parameters, and shaping exponents, respectively [19]. Moreover, $d_3 = f_i(< Y^*_{3,max} - Y_{02} >)$, since the martial is assumed to be transversely isotropic (in-plane symmetry $Y_{02} = Y_{03}$). The parameters introduced into the damage evolution equation (Eq 17) offer a range of possibilities enough to describe the kinetics of damage evolution while retaining the saturation behavior corresponding to experimental observations [19]. The a_i parameters represent the saturation values or the maximum attained values for distributed damage before failure. The parameters b_i and c_i have unique effects on shaping the material's non linear behavior. The exponent c_i has an influence on the shape of damage kinetics; indeed ifc_i is closer to 1 the nonlinear curve will have an "S" shape as shown in Figure 2 for $\theta = 45°$, while for smaller c_i values the curve will look more like a "hook" shape as show in Figure 2 for $\theta = 0°$. On the other hand, the normalizing thermodynamic force parameter b_i determines how fast does the curve attains its damage saturation

value, where for smaller b_i values the material tends to reach damage saturation at a faster rate.

2.2. *Model Calibration*

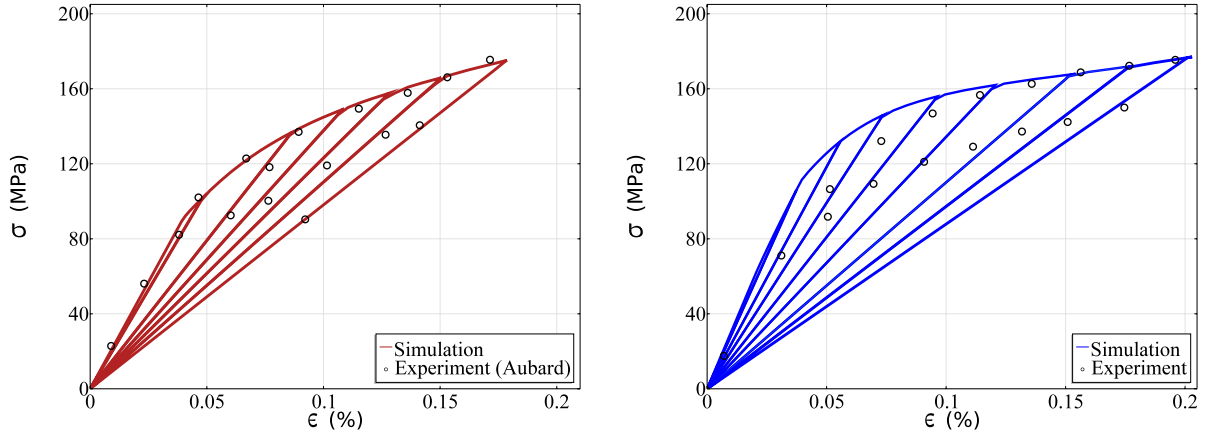

Figure 2: Experimental [24] and Finite Element (FE) simulations of nonlinear incremental loading/unloading stress vs strain curves of SiC/SiC samples at left: $\theta = 0°$ Right $\theta = 45°$ fiber orientations

The present model is phenomenological, developed along the spirit of continuum plasticity theory, where microstructure details are ignored. It is thus predictive only as far as it is validated with experimental data and its parameters are uniquely determined. The model was validated with uniaxial cyclic tensile tests at different fiber orientations, from which all model parameters were obtained.Then a validation with a multi-axial problem was established. The developed damage model parameters shown in Table 2 were determined using the experimental data of Aubard and co-workers [24] since their experimental data base is sufficient to determine model parameters (parameter identification), and then for validation through independent tests. The data base for nuclear grade SiC/SiC is scarce at present, and future efforts may be directed towards parameter identification for nuclear grade SiC/SiC. The results of model calibration are shown in Figure 2 for $0°$ and $45°$ fiber orientations. The uniaxial test calibration determines a set of model parameters (model identification) that were then used for further validation of a pressurized tube test, where multiaxial loading is present. The results of model comparison with experiments are shown in Figure 3, where the agreement is quite good.

Table 2: Damage model parameters

	Parameters	**Symbol**	**Value**	**Unit**
Damage evolution law parameters d_2	Initial damage threshold	Y_{02}	0.0182	MPa
	Fitting parameters	a_2, c_2	0.8 , 0.8377	N/A
	Normalizing thermodynamic Force	b_2	0.117	MPa
Damage evolution law parameters d_4	Initial damage threshold	Y_{04}	0.0396	MPa
	Fitting parameters	a_4, c_4	0.9 , 0.8685	N/A
	Normalizing thermodynamic force	b_4	0.4567	MPa
Damage coupling functions g_{24}, g_{42}	Constant parameter g_{24}	a_{24}	5.958	N/A
	Exponent parameter g_{24}	b_{24}	1.221	N/A
	Constant parameter g_{42}	a_{42}	6.612	N/A
	Exponent parameter g_{42}	b_{42}	0.9544	N/A

In order to increase the validity domain, it is necessary to measure the model's ability to predict the mechanical behavior of SiC/SiC when the stress state is different from those used

in the identification procedure. Finite Element (FE), using the commercial code COMSOL, computer simulations of biaxial tests preformed by [24] on SiC/SiC of pressurized thin tubes were established and compared to Aubard's experimental data (Figure 3). The simulation results show good agreement with the general behavior of the tested thin pressurized tubes. However, we note that the SiC/SiC material used in pressurized tubes exhibit a stiffer behavior than the material used for the uniaxial tests. The experiential data for the axial and hoop stress-strain curves show good agreement with the present model. Thus, we will proceed now to apply the damage model to the more complex situation in which SiC/SiC is used as fuel cladding under complex thermo-mechanical loading, coupled with irradiation effects.

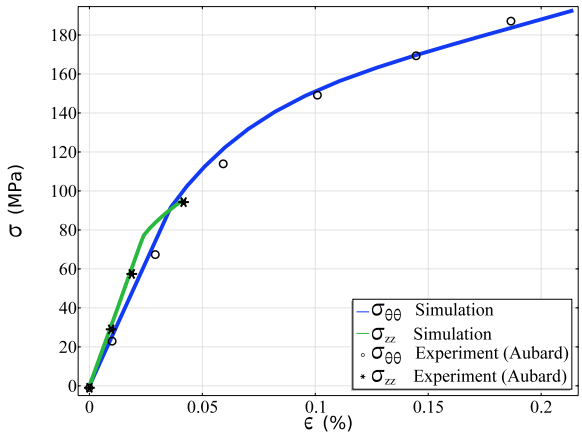

Figure 3: Experimental ([24]) and FE simulations of a pressurized SiC/SiC thin-walled tube test.

2.3. Radiation Effects

Neutron irradiation influences the thermal and mechanical properties of SiC composites in several critical areas. First, it leads to volumetric swelling through the accumulation of nano-size interstitial clusters, voids and helium-filled bubbles. Then, the thermal conductivity of the composite material is degraded as a result of defect accumulation, and finally, the matrix cracking threshold is also reduced. The effects of neutron irradiation on the mechanical and thermal properties of SiC/SiC composites have been extensively reviewed in references [3, 4, 16, 25]. In the present model, we include the dependence of swelling, thermal conductivity, and strength, on the irradiation dose and temperature following recent literature[2].

Volumetric Swelling: Swelling in the SiC/SiC fuel cladding is a function of temperature and irradiation dose, which can be described by the following equation [2]

$$\dot{e} = k_s \gamma^{-1/3} \exp(-\frac{\gamma}{\gamma_{sc}}) \tag{18}$$

where k_s is a temperature-dependent rate constant, γ is the neutron fluence in dpa units and γ_{sc} is a characteristic fluence. These are related to temperature T as [2]:

$$\begin{aligned} k_s(T) &= 0.10612 - 1.5904 \times 10^{-4} T + 6.0631 \times 10^{-8} T^2 \\ \gamma_{sc}(dpa) &= 0.51801 - 2.7651 \times 10^{-3} T + 9.4807 \times 10^{-6} T^2 - 1.3095 \times 10^{-8} T^3 \\ &\quad +6.7221 \times 10^{-12} T^4 \ \ (473K < T < 1074K) \end{aligned}$$

By numerically integrating Eq (18) at different temperatures, one can obtain values of the volumetric swelling as function of irradiation dose. An interpolation of the data obtained from Eq (18) was preformed in order to obtain the amount of swelling at each time step during the simulation of damage evolution. This is based on the assumption that the time scale for variation of swelling due to a change in temperature is much shorter than the time scale for temperature evolution in the cladding during operation[2], or during transients. In this work, swelling build up will only be considered for normal operating conditions of nominally 2 years. On the other hand, during off-normal operating conditions, swelling will be assumed to be constant, since the time for an off normal transient is relatively small (40 minutes [26]).

Thermal conductivity: The thermal conductivity of SiC/SiC CMC undergoes significant changes as function of temperature and irradiation dose. Neutron irradiation results in an initial steep drop in the conductivity as a function of irradiation fluence as a result of defect accumulation and their influence on phonon scattering [2]. The value of the thermal conductivity changes rather slowly after this initial drastic change. According to Singh et. al [2], the thermal conductivity can be obtained by taking the reciprocal of the thermal resistivity ($k = \frac{1}{R_0+R_{rd}} = \frac{1}{R_{irr}}$).

$$R_{irr} = R_0 + R_{rd} \tag{19}$$

where R_{irr} $(\frac{m\ K}{W})$ is the thermal resistivity of the irradiated material, R_0 $(\frac{m\ K}{W})$ is the thermal resistivity of the unirradiated material, and R_{rd} $(\frac{m\ K}{W})$ is the defect thermal resistivity.

$$R_0 = \frac{190.32\ T + 36684}{\rho_0 C_p}$$

where ρ_0 $(\frac{kg}{m^3})$ is density and C_P $(\frac{J}{kg\ K})$ is the specific heat capacity of SiC/SiC, which is a function of temperature and can be written as: $C_p = 925.65 + 0.3772T - 7.9259 \times 10^{-5}T^2 - 3.1946 \times 10^6 T^{-2}$. The defect thermal resistivity is simply related to the volumetric swelling strain as [2]:

$$R_{rd} = 14.275\ \frac{e}{3} \tag{20}$$

Finally, It was found that the effect of neutron irradiation on the coefficient of thermal expansion (CTE) is not significant [2], Thus the CTE is known to increase with temperature and can be written as: $\alpha(10^{-6}/K) = -0.7765 + 1.4350 \times 10^{-2}T - 1.2209 \times 10^{-5} + 3.8289 \times 10^{-9}T^3 \quad (293 < T < 1293K)$.

2.4. Finite Element Multiphysics Model Description

Full FE-based multiphysics computer simulations were conducted to study the influence of various potential reactor operational scenarios on the non-linear mechanical response of SiC/SiC fuel cladding. This has been accomplished using the commercial FEM code COMSOL, where coupling between three types of physics has been achieved, as shown in Figure (4): thermomechanics, heat transfer, and damage evolution. The simulation modules for solid mechanics and heat transfer (commercial) have been coupled with an additional system of ordinary differential equations that include damage evolution as function of thermodynamic forces. The contributions of the current study are summarized within the gray boxes and the arrow couplings in the figure. The cladding geometry was simplified by taking advantage of its symmetry, where only a quarter of the cladding was modeled and the cap geometry was simplified as shown in

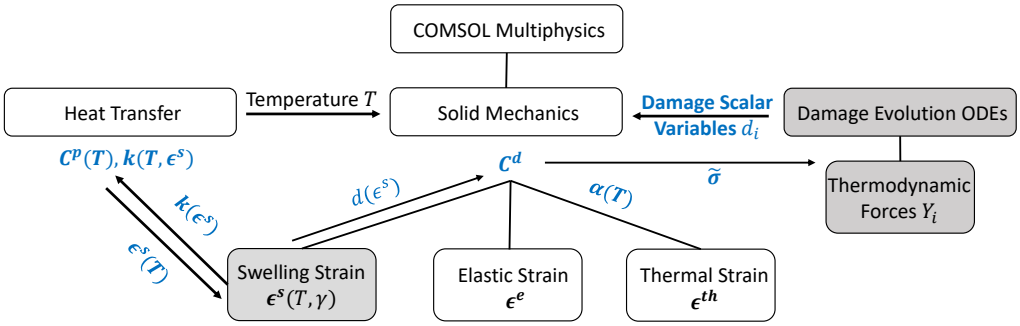

Figure 4: Schematic of the multiphysics model implementation procedure

Figure (5). The axial length of the cladding was taken to be the top 28 mm close to the cap, while keeping the heat flux distribution along the axial length. The fuel cladding geometry and reactor operating parameters are based on the Seabrook reactor parameters shown in Table (3), and used in Carpenter's analysis [6].

The model was meshed with 2-D elements on the surface, and then swept over the circular cross section to obtain the 3-D mesh with more elements though the thickness for better accuracy.

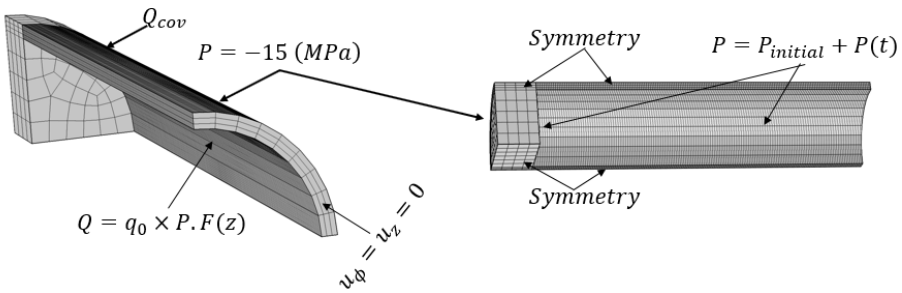

Figure 5: Meshed SiC/SiC cladding model with boundary conditions

3. Reactor Operational Scenarios

The SiC/SiC-based fuel cladding was subjected to two main analyses with two different operating conditions: normal and off-normal.In the analysis of normal operations, the fuel cladding is assumed to be operating for 2 years [6], since the evolution and saturation of swelling occurs during the early stages (4 months) of the cladding life (typically 4 years). Once damage saturation occurs, material properties are no longer subject to change and the stress levels become steady and do not increase. However, due continuous fission gas release, the internal pressure keeps on building up, thus raising stress levels to higher tensile values in the cladding [2]. This, in turn, was taken into account by assuming a linear increase in pressure with neutron fluence. The implemented constitutive model of SiC/SiC took into account elastic strain, thermal strain, volumetric swelling, and associated damage, as presented in section 2.Two pressure boundary loads were imposed on both the inner and outer surfaces of the cladding, as shown in the Figure (5). The inner pressure was linearly increased (proportional to irradiation fluence) from 2.41 MPa to 23 MPa, over a two-year period, while the external pressure was kept

constant at 15.51 MPa on the outer cladding surface to simulate water coolant pressure [6]. A fixed displacement boundary condition was applied to the bottom surface of the fuel cladding (because of the long length of the fuel rod), while symmetry boundary condition was imposed on the surfaces shown in Figure (5). The heat generated from the fuel pellets was assumed to give off a heat flux of 1.33 MW/m^2 at the inner surfaces of the cladding, as shown in Figure (5). Since the heat flux varies, a peaking factor function of the cladding height was applied [2]. External cooling was considered by applying a convective heat flux with a typical heat transfer coefficient of 30 kW/m^2.K and 580 K bulk coolant temperature[2]. The irradiation dose was assumed to increase linearly over the operating time of 2 years from 0 to 6 dpa[2].

Off-normal operating conditions are characterized by loss of cooling at the end of 2 years

Table 3: Parameters describing the fuel cladding in the Seabrook nuclear reactor [6].

Parameter	Units	Value
Cladding outer radius	mm	4.75
Cladding thickness	mm	0.571
Radial gab thickness	mm	0.825
Internal gas pressure	MPa	2.41
Coolant pressure	MPa	15.51

of normal operations. Loss of cooling was simulated by imposing a gradual linear degradation function to the heat transfer coefficient, reducing it from 30 kW/m^2.K to 0.96 kW/m^2.K, during a 40-minute duration according to the international atomic energy agency's report on Fukushima and Diacchi nuclear accident analysis[26]. The report estimated the time for the core to be completely uncovered from the initial time of the loss of cooling. Moreover, swelling evolution was kept constant at the accumulated value at the end of 2 years of normal operating conditions.

Cold shutdown was implemented for both main operating scenarios, where the heat flux was linearly reduced to zero over a short period of time, while the volumetric strain was kept constant. This is because the cold shutdown time is relatively short, and does not impact the accumulated swelling strain. In summary Three major reactor operating scenarios were considered in this analysis

- Normal operating conditions
- Cold shutdown
- Off-normal operating conditions

4. Results

4.1. Normal Operating Conditions

Figure (6) shows the development of the axial (right) and hoop (left) stress in the cladding over the two-year operating period. It is shown that at the beginning of the cladding life (t$<$ 2 months), the inner surface is under higher compressive stress compared with the outer surface

Table 4: Assumed reactor operating scenarios [6].

Parameter	Normal operating condition	Cold Shutdown	Off-normal operating condition
Operating Period	24 months	N/A	40 minuets
Fluence (dpa)	0-6	6	6
Linear heating rate (kW/m^2.K	30	0	30
Operating coolant temperature (K)	580	323	N/A
Operating coolant pressure (MPa)	15.51	12	15.51
Operating internal pressure (MPa)	2.41-23	23	23

(Figure 7). This is due to the fact that the inner surface is at a higher temperature tending to expand faster than the outer surface, and because of self-constraint, it displays larger compression stress as compared to the outer surface because of the coolant pressure. As the cladding is irradiated over longer periods of time, it starts to experience volumetric swelling. The swelling rate is higher in cooler regions of the cladding [2], and thus the outer regions will expand faster than the inner regions, reversing the effects of thermal expansion alone. This effect is shown in Figure 7, where the inner surfaces are under higher tensile stress as compared to the outer surfaces. When the swelling reaches saturation, the difference between the stress values in the inner and outer regions will become steady. However, because of the continuous increase in the internal fission gas pressure, the stress difference will continue to increase, even after the swelling saturates. Since the magnitude of the tensile stresses achieved at the end of 18 months is less than the matrix micro-cracking stress of SiC/SiC, no significant damage occurs during the first 18 months of operation. The small amount of damage accumulated beyond 18 months is due to biaxial loading effects, as shown in Figure (7). It is worth mentioning that microcracking was noticed in SiC/SiC specimens, even before reaching the microcracking stress limit through measurements of acoustic energy vs load in simple tensile tests [2].

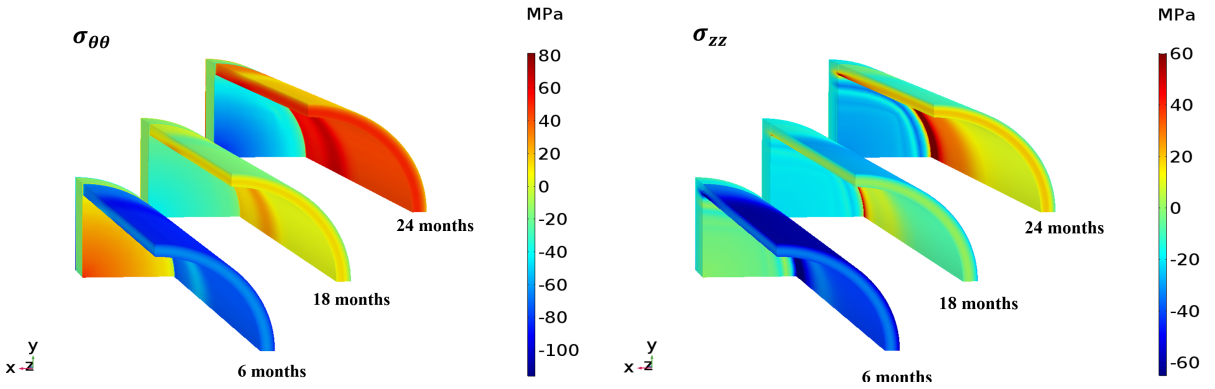

Figure 6: Spatial distribution of tangential and axial stress $\sigma_{\theta\theta}$ & σ_{zz}, respectively, at the end of 6, 16, and 24 months of operation.

The cladding outer surface temperature quickly reaches a steady-state value of 627 K. However, the inner surface temperature increases gradually until it reaches steady-state at 740 K. The increase and saturation of temperature is explained to be due to the influence of swelling on reduction of the thermal conductivity. Moreover, a varying heat flux as a function of the cladding axial length results in creating a region where stress components are maxima, as shown in Figure (8). The reason behind the emergence of such a region near the end plug is because the

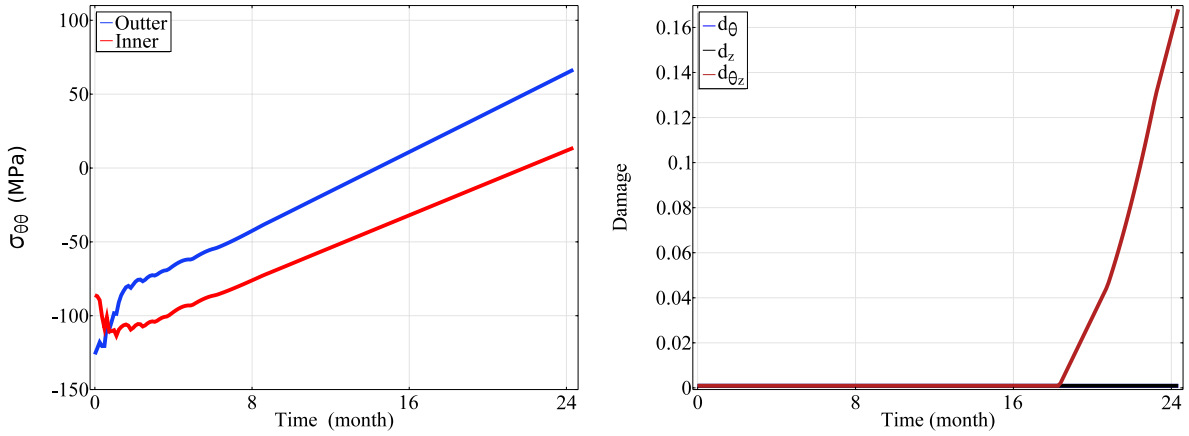

Figure 7: Variation of the tangential stress and corresponding damage parameters over a 2-year period at an axial plane close to the end plug

heat flux decreases according to the peaking factor function. This results in a decrease in the axial temperature in this region, which finally causes relatively larger swelling combined with higher thermal strains. This combination of volumetric and thermal strains eventually creates a maximum stress region, as shown in Figure (8). The figure also shows that at the intersection point between the normalized temperature and swelling values, a local-global stress maximum occurs.

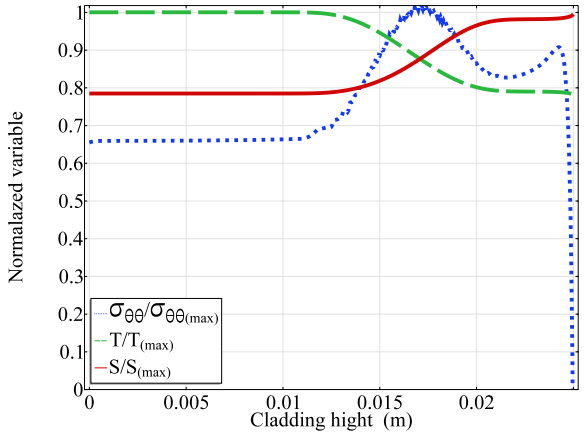

Figure 8: Variation of the normalized hoop stress, temperature and swelling along the cladding axial length at the end of its life.

4.2. Off-normal Operating Conditions

Results from the last time step in the previous analysis of normal operating conditions were then used as input to the analysis of a hypothetical off-normal operating scenario. Thermal strains are considered as the main deformation contributor during off-normal operating conditions, since swelling is constant during the relatively short off-normal transient of 40 minutes. Initially, the cladding experiences lower tensile and compressive stresses (axial & hoop) at the inner and outer regions, as shown in Figure (6). After approximately 35 minutes, the outer and inner surface stresses change to higher tensile hoop and compressive axial stress, respectively, as shown in Figures (9). Larger tensile and compressive stresses increase on the outer and in-

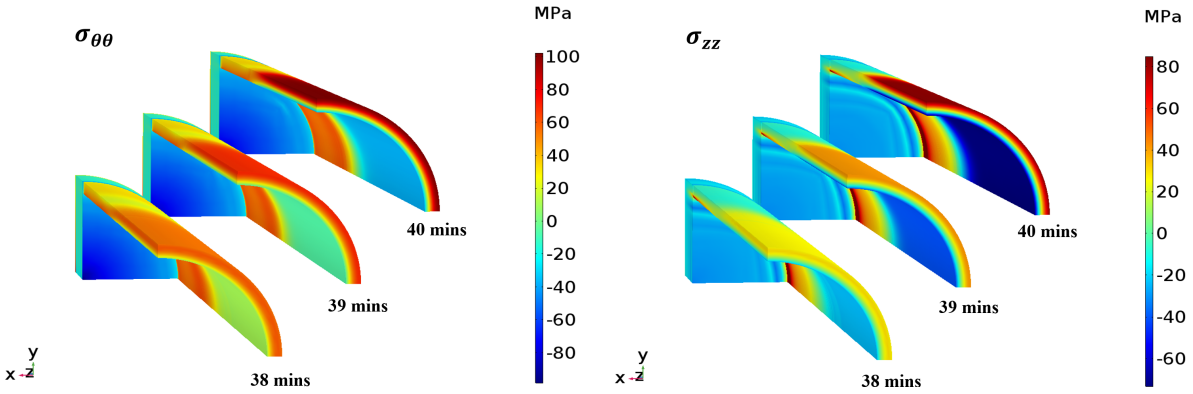

Figure 9: Tangential and axial stress $\sigma_{\theta\theta}$ & σ_{zz} (MPa) distribution during off-normal operating conditions.

ner regions until approximately 39 minutes. Then the cladding experiences significant damage accumulation, which starts from the outer region and keep on progressing towards the inner regions, as shown in Figure (11). The damage associated with the tangential principal direction is approximately similar to that associated with the axial direction due to the assumption that fibers are parallel and perpendicular to the axial direction (0/90), giving the composite a transversely isotropic structure. Figure (10) shows that most of the damage occurs in the region

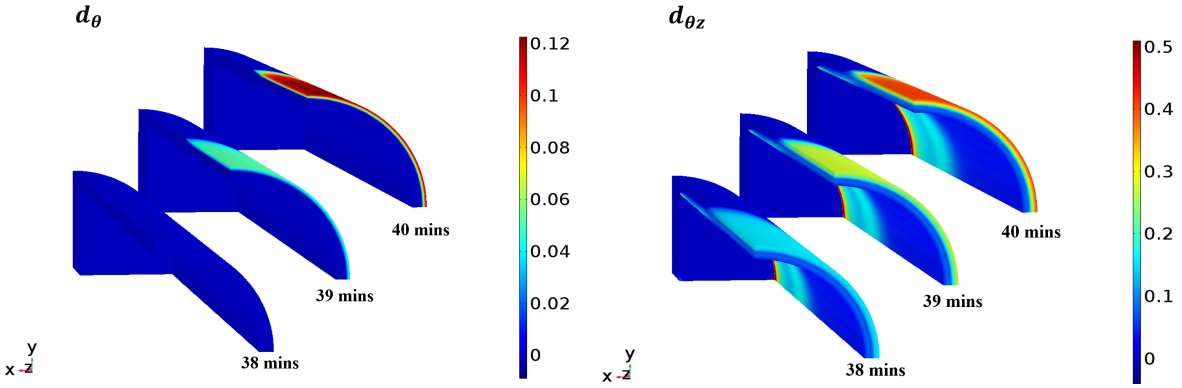

Figure 10: Evolution of the damage parameter components (d_θ) & $(d_{\theta z})$ during off-normal operating conditions

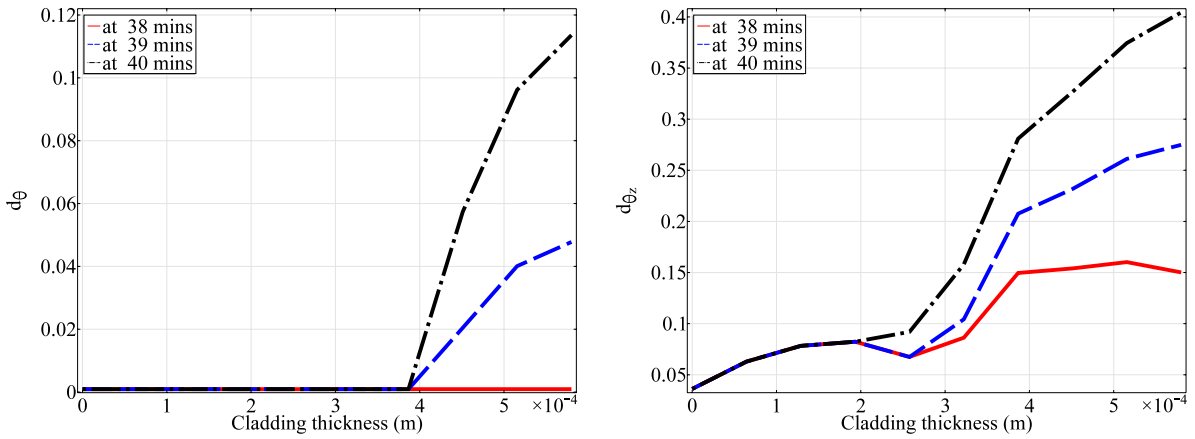

Figure 11: Damage variable evolution (d_θ) & $(d_{\theta z})$ at the end of the off-normal operating transient.

where the heat flux is maximum, indicating that at off-normal conditions, the damage is driven by thermal stresses caused by loss of cooling. As the cladding temperature increases in the presence of irradiation, the thermal conductivity in decreases, leading to a larger temperature gradient, which becomes steeper after 30 minutes from the beginning of the transient (Figure 12). It should be noted that some of the thermal conductivity will likely to be recovered due to the annihilation of vacancies at high temperature in absence of irradiation.

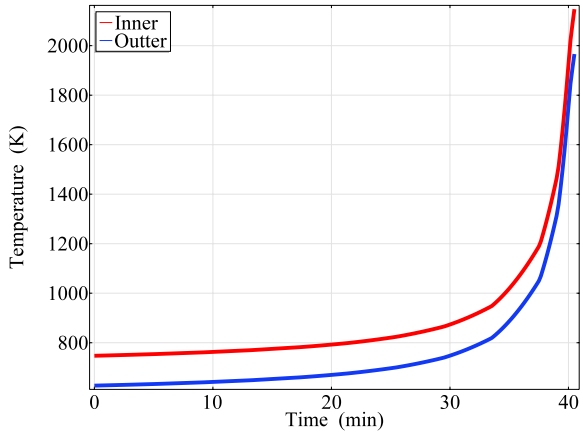

Figure 12: Temperature evolution of the inner and outer surfaces in the cladding during off-normal operating conditions.

4.3. Cold Shutdown

During the reactor's cold shut down, the fuel cladding will be subjected to high tensile stress at the inner regions as a result of the accumulated swelling strain, which has an opposing and dominant effect on thermal expansion. Thermally induced strains vanish after reactor's cold shutdown because temperature gradients decrease to negligible values allowing the accumulated swelling to drive tensile stresses at the inner surfaces to even higher magnitudes. This, in turn, can cause higher failure probability, while the outer regions remain at compressive or low tensile stresses values. Moreover, the inner and outer pressure difference plays a significant rule in either decreasing or increasing tensile stresses. Having a compressive pressure difference will obviously decrease the tensile stress at the inner surface. However, during the reactor's cold shutdown, the coolant is depressurized leading to even higher tensile stresses that might cause failure at the inner regions of the SiC/SiC fuel cladding.

The effects of the reactor's shutdown conditions were investigated in the following operational scenarios at normal operating conditions:

1. Initial gab pressure of 2.41 MPa (He gas);
2. Reduced thermal conductivity (40% decrease);
3. Initial Liquid Netal (LM) gab pressure of 0.1 MPa.

The above operating scenarios consist of a nominal case represented with an initial gab pressure of 2.41 MPa compared with a decreased thermal conductivity case and a case where the gab has a liquid metal instead of Helium gas. These cases will be discussed in details in section5. Each operating scenario was simulated for 2 years until saturation and final internal and irradiation dose values are reached, then each case was subjected to cold shutdown conditions. These conditions were simulated by decreasing the heat flux gradually and the coolant

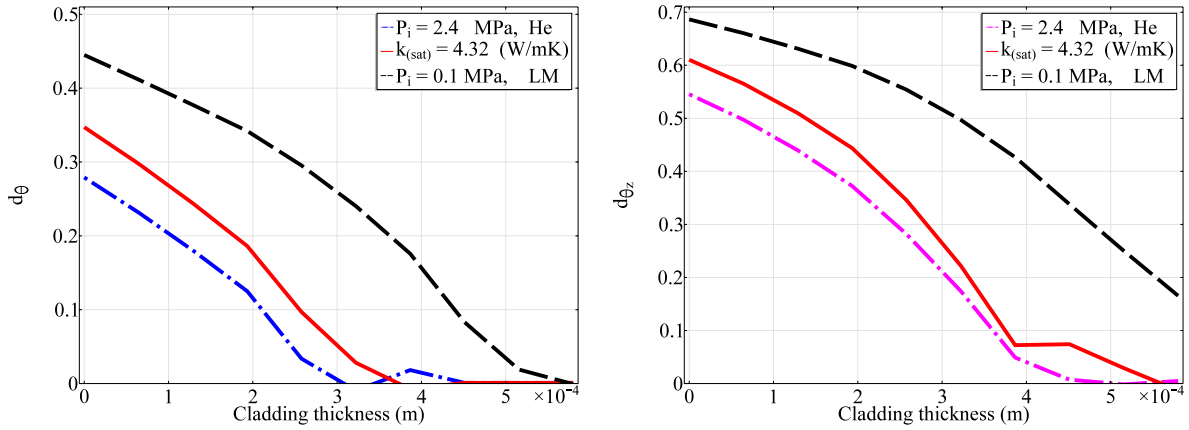

Figure 13: Damage parameter evolution (d_θ) & $(d_{\theta z})$ after shutdown for different loading scenarios

temperature to zero and 323 K, respectively, along with an incremental depressurization of the coolant by an average pressure of 3 MPa in a relatively short period of time [11]. The accumulated swelling was kept constant. The first operating scenario was chosen to be the nominal case that matches the work of Singh et. al [2], while the last two cases were the extreme cases of thermal conductivity variation and initial gab pressure.

Unlike off normal operating conditions, damage evolution will propagate from the inner surfaces to outer regions for the three different operating scenarios.It is obvious from Figures (13&14)that the most extreme scenario is when using liquid metal as an alternative in fuel-cladding gab which will result in subjecting the whole fuel pin thickness to tensile stresses and high damaging effects.

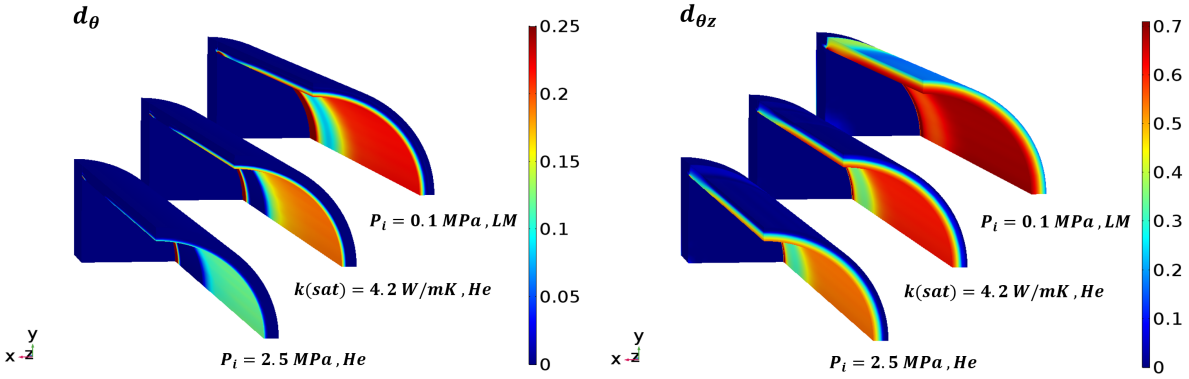

Figure 14: Damage d_θ & $d_{\theta z}$ after shutdown at different operating scenarios

One can conclude from these studies that the most extreme loading cases will occur after the reactor's cold shutdown, which will result in severe damaging effects to the inner cladding regions. The damage model was able to capture the non-linear behavior across the cladding thickness, as shown in Figure (15), even for the nominal case where previous elastic studies indicated purely elastic linear cladding response during normal operating conditions[2]. Here, we see that the fuel cladding has obviously exceeded the proportional limit for matrix micro-cracking, and that the non-linear behavior was captured by the present model.

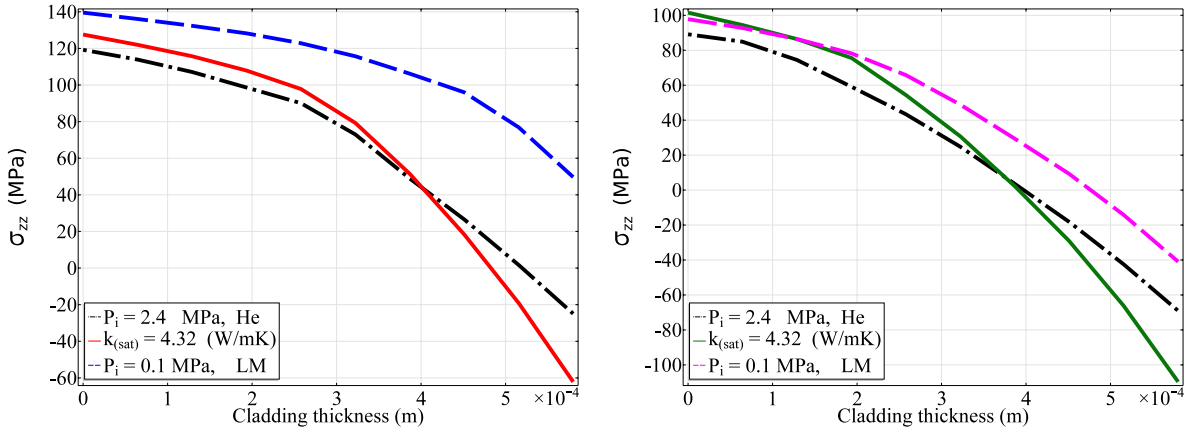

Figure 15: Tangential and axial stress ($\sigma_{\theta\theta}$&σ_{zz}) variation across the fuel cladding thickness after shutdown for different operating scenarios

5. Impact of Gap Pressure Uncertainty

The gap between the fuel pellets and the cladding is considered as a critical design parameter. Traditionally, when zircaloy cladding is used, the fuel pellet expands due to fission gas swelling, which closes the initial fuel-cladding gab and results in additional contact stress and significant creep deformation. However, in the case of SiC/SiC-cladding where creep is negligible, the possibility of the gab being closed under reasonable initial gab thickness is significantly low [2]. Analysis carried out by Ben-Belgacem et. al [7] showed that the cladding with an initial gab thickness larger than 30 μm will not close for fuel 60 MWd/kg burnup.

The initial gap is also important when it comes to reducing fuel temperature. It is usually filled with helium gas due to its inert nature, low neutron absorption and high thermal conductivity when compared to other gases. Gas conductance can be optimized by increasing the initial gas pressure, which will help in decreasing the fuel temperature according to FRAPCON analysis done by Carpenter [6]. Moreover, An alternative to helium gas is liquid metal bonds (LM), such as sodium and potassium alloys. Using these metals will have a significant effect in decreasing the fuel temperature up to 160 °C when compared to He gas. However, one disadvantage is the accumulation of higher internal pressure as time progresses. Since creep is negligible in the case of SiC/SiC cladding, one can consider such an alternative by conducting an analysis on the effects of an increase in the internal pressure on the cladding.

A simulation was conducted comparing a nominal 2.41 MPa initial He gas pressure to two additional cases based on a 60% increase (4 MPa) in the initial gas pressure, and another case using LM as an alternative. Pressure values for each case were obtained from an earlier analysis done with FRAPCON [6].

Normal operating conditions:

Changing in the gab conditions did not have a significant impact on temperature distributions. However, the tangential and axial stresses were significantly changes, as shown in Figure (16). During normal operating conditions, an increase in the initial pressure resulted to an increase in inner and outer stress, when compared to the case with a nominal initial He gas pressure. The results of this sensitivity analysis are shown in Figure (16).

Moreover, the largest increase in both tangential and axial stresses was obtained when liquid metals were used as an alternative to helium. Although the initial pressure for this case was low,

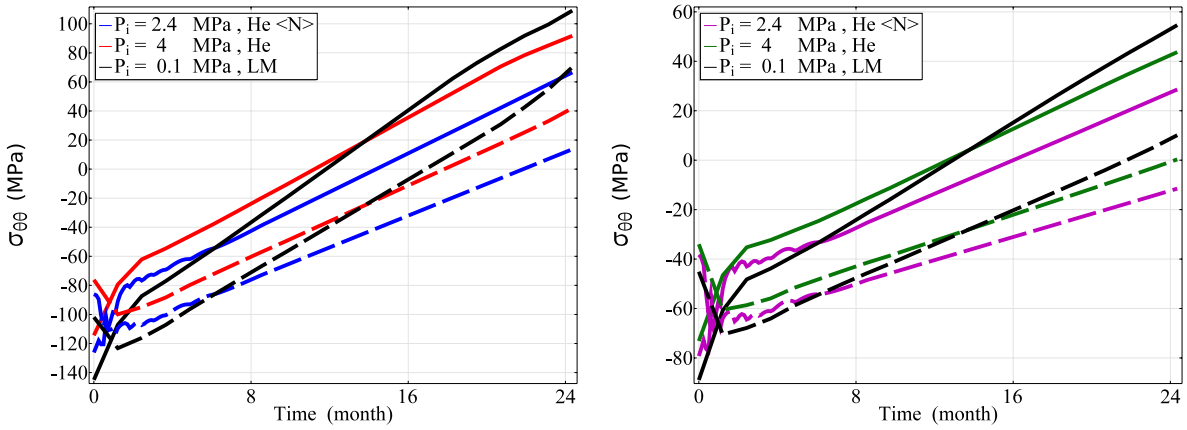

Figure 16: Evolution of cladding tangential and axial stress $\sigma_{\theta\theta}$ & σ_{zz} (MPa), with an increase in the initial gab pressure, or when LM is used as an alternative. The solid lines indicate stresses at the inner surface, while the dashed lines indicate stresses at the outer surfaces of the cladding

however, and over time, internal pressure built up to 30 MPa over the period of operation [6]. This increase results in accumulating damage in both the inner and outer regions, as shown in Figure (17), where the largest damage accumulation is noted in the LM case. The inner surfaces are more affected, as illustrated, where the increase in stress will eventually lead to damage accumulation, even for normal operating conditions.

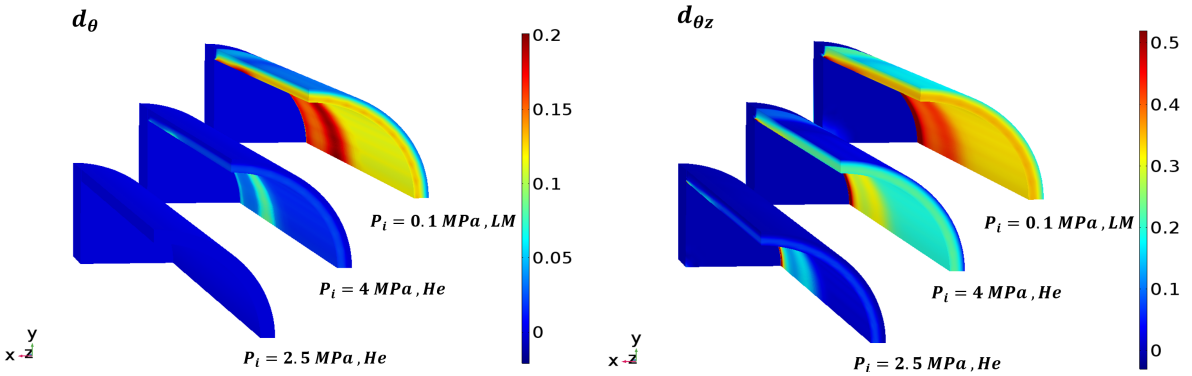

Figure 17: Damage components (d_θ) & $(d_{\theta z})$ during normal operating conditions at different initial gab pressures and conditions.

Off-normal operating conditions:

During off-normal operating conditions, where thermal strain is the main deformation mechanism, an increase in the internal pressure results in more damaging effects to the outer regions of the cladding, as shown in Figure (18). As time progresses during a loss of cooling accident, more tensile thermal stress accumulates on the outer surfaces which increases the already high tensile stress due to the internal pressure, and causes severe damage accumulation.

6. Conclusions

Recent developments of SiC/SiC CMC fuel cladding materials has opened the door to the possibility of more accident-tolerant fission reactors. Understanding the influence of key parameters on cladding design is an issue that should be addressed, especially in assessing the influ-

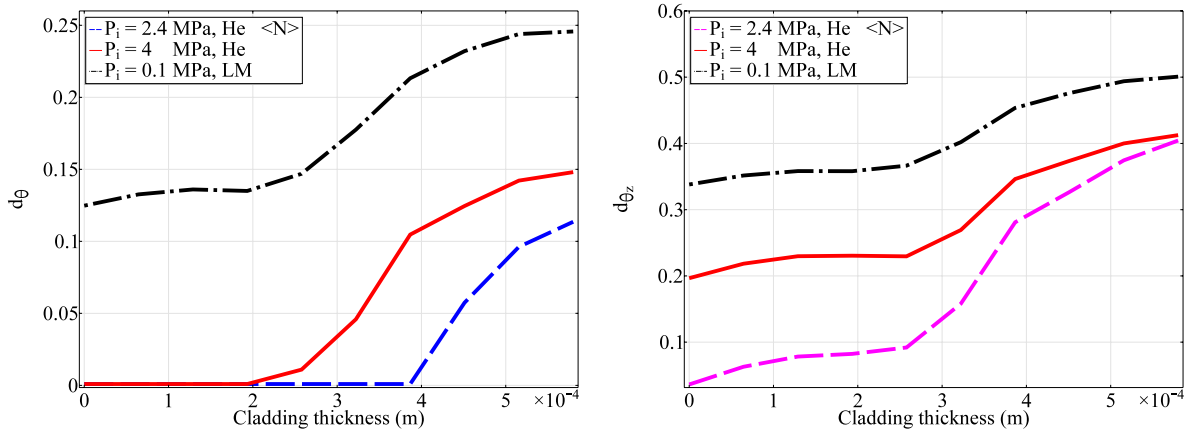

Figure 18: Damage parameter evolution (d_θ) & $(d_{\theta z})$ for different initial gab pressures during off-normal operating conditions.

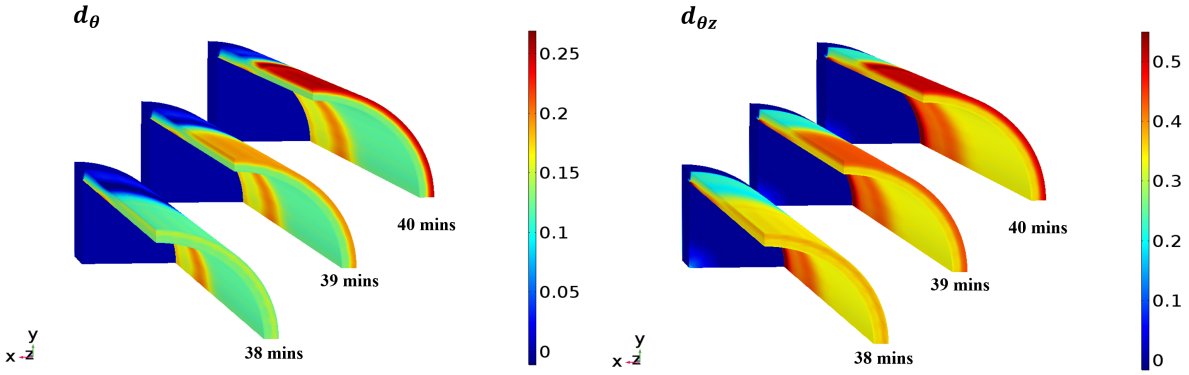

Figure 19: Damage (d_θ) & $(d_{\theta z})$ during off-normal operating conditions at $P_i = 0.1$ (MPa) of LM

ence of scenarios that impose high stresses exceeding conventional elastic limits. The present study provides an understanding of the effects of the non-linear thermo-mechanical behavior on the stress and damage state of the cladding during normal, off-normal, and cold shutdown conditions. Boundary conditions for each scenario were obtained from a previously conducted fuel performance analyses by Carpenter [6], and the International Atomic Energy Agency's report on Fukushima and Diacchi nuclear accident[26]. With the help of the developed non-linear damage model, the SiC/SiC based cladding mechanical behavior due to high multi axial thermo-mechanical loads is described. This leads to complete determination of spatial damage distributions in the cladding indicating possible regions of failure or large-scale crack initiation.

In ceramic matrix composites the material exhibits high porosity (up to 20% [16]) where the distributed pores are considered as pre-existing flaws in SiC/SiC CMC since they form potential regions to initiate matrix micro cracking upon loading. The presence of distributed damage in the form of porosity or micro-cracks does not necessarily mean failure, and should be considered within the design guidelines. For example, in metallic structures under thermal creep conditions, grain boundary type micro-voids are tolerated, up to about a strain of 1%. Design codes for SiC/SiC should be based on design-by-analysis, as in the current study, where a limit is set for the damage parameter around 0.1-0.2, before replacement is recommended. Since strain to failure is roughly seven times larger than the strain at which SiC/SiC CMC starts to micro-crack, one has to take an advantage of such a deformation. An accumulated damage

threshold should be set in order to determine the maximum amount of damage that can be achieved while the structure preserves its integrity under the fuel cladding operating conditions including irradiation effects. With the implemented damage model, one can determine the lifetime of the fuel element, including the influence of operational and off-normal scenarios.

When comparing damage induced by the increase in internal pressure to damage due to variability in the of thermal conductivity, it is obvious that the pressure increase has a more damaging effect. Fuel-cladding gab conductance enhancement using LM will not only damage the outer surfaces, but it will also induce damage to the inner surfaces putting the fuel cladding under a completely micro-cracked state due to the large increase in the internal pressure caused by filling the space around the pellet with liquid eutectic and reducing the free gas volume by 50% [6]. However, when comparing the damage severity or magnitude, for a 100% increase in the final internal pressure, the maximum damage obtained at the outer surface was found to be $d_{\theta z} = 0.5$, which is less than the maximum damage obtained form a 40% decrease in the thermal conductivity ($d_{\theta z} = 0.6$). This illustrates that SiC/SiC cladding damage severity is more sensitive to thermal conductivity variations than to uncertainties in the initial gab conditions.

The emergence of SiC/SiC CMC in nuclear applications will help to create safer and more efficient reactors by replacing conventional Zr-based cladding. The analysis done in this work shows that a prediction in the cladding damage can give an upper limit for designers to develop more reliable and safer fuel cladding systems.

7. Acknowledgments

The project was partially funded by Kuwait Foundation for the Advancement of Sciences (KFAS) under project code CB18-65EM-02. The authors wish to acknowledge the support of the U.S. Department of Energy, Office of Fusion Energy, through the DOE award number DE-SC0018410 at UCLA.

References

[1] Kurt A Terrani, Bruce A Pint, Chad M Parish, Chinthaka M Silva, Lance L Snead, and Yutai Katoh. Silicon carbide oxidation in steam up to 2 mpa. *Journal of the American Ceramic Society*, 97(8):2331–2352, 2014.

[2] Gyanender Singh, Kurt Terrani, and Yutai Katoh. Thermo-mechanical assessment of full sic/sic composite cladding for lwr applications with sensitivity analysis. *Journal of Nuclear Materials*, 499:126–143, 2018.

[3] Yutai Katoh, Kazumi Ozawa, Chunghao Shih, Takashi Nozawa, Robert J Shinavski, Akira Hasegawa, and Lance L Snead. Continuous sic fiber, cvi sic matrix composites for nuclear applications: Properties and irradiation effects. *Journal of Nuclear Materials*, 448(1-3):448–476, 2014.

[4] Yutai Katoh, Takashi Nozawa, Lance L Snead, Kazumi Ozawa, and Hiroyasu Tanigawa. Stability of sic and its composites at high neutron fluence. *Journal of Nuclear Materials*, 417(1-3):400–405, 2011.

[5] Eugene van Heerden, Chan Y Paik, Sung Jin Lee, and Martin G Plys. Modeling of accident tolerant fuel for pwr and bwr using maap5. 2017.

[6] David Michael Carpenter. *An assessment of silicon carbide as a cladding material for light water reactors*. PhD thesis, Massachusetts Institute of Technology, 2010.

[7] M Ben-Belgacem, Victor Richet, Kurt A Terrani, Yutai Katoh, and Lance Lewis Snead. Thermo-mechanical analysis of lwr sic/sic composite cladding. *Journal of Nuclear Materials*, 447(1-3):125–142, 2014.

[8] G Singh, R Sweet, NR Brown, BD Wirth, Y Katoh, and K Terrani. Parametric evaluation of sic/sic composite cladding with uo2 fuel for lwr applications: fuel rod interactions and impact of nonuniform power profile in fuel rod. *Journal of Nuclear Materials*, 499:155–167, 2018.

[9] Weiping Lan, Dachao Lin, Zulong Hao, and Fenglei Niu. Stress analysis of three-layer sic cladding for pwrs. In *2017 25th International Conference on Nuclear Engineering*, pages V003T02A032–V003T02A032. American Society of Mechanical Engineers, 2017.

[10] Yangbin Deng, Koroush Shirvan, Yingwei Wu, and Guanghui Su. Probabilistic view of sic/sic composite cladding failure based on full core thermo-mechanical response. *Journal of Nuclear Materials*, 507:24–37, 2018.

[11] JG Stone, R Schleicher, CP Deck, GM Jacobsen, HE Khalifa, and CA Back. Stress analysis and probabilistic assessment of multi-layer sic-based accident tolerant nuclear fuel cladding. *journal of nuclear materials*, 466:682–697, 2015.

[12] Malik Wagih, Benjamin Spencer, Jason Hales, and Koroush Shirvan. Fuel performance of chromium-coated zirconium alloy and silicon carbide accident tolerant fuel claddings. *Annals of Nuclear Energy*, 120:304–318, 2018.

[13] Valentina Angelici Avincola, Pierre Guenoun, and Koroush Shirvan. Mechanical performance of sic three-layer cladding in pwrs. *Nuclear Engineering and Design*, 310:280–294, 2016.

[14] Sumio Murakami. *Continuum damage mechanics: a continuum mechanics approach to the analysis of damage and fracture*, volume 185. Springer Science & Business Media, 2012.

[15] JP Cordebois and F Sidoroff. Damage induced elastic anisotropy. In *Mechanical Behavior of Anisotropic Solids/Comportment Méchanique des Solides Anisotropes*, pages 761–774. Springer, 1982.

[16] Lance L Snead, Takashi Nozawa, Yutai Katoh, Thak-Sang Byun, Sosuke Kondo, and David A Petti. Handbook of sic properties for fuel performance modeling. *Journal of nuclear materials*, 371(1-3):329–377, 2007.

[17] Yutai Katoh, Takaaki Koyanagi, Joel L McDuffee, Lance L Snead, and Ken Yueh. Dimensional stability and anisotropy of sic and sic-based composites in transition swelling regime. *Journal of Nuclear Materials*, 499:471–479, 2018.

[18] JF Maire and JL Chaboche. A new formulation of continuum damage mechanics (cdm) for composite materials. *Aerospace Science and Technology*, 1(4):247–257, 1997.

[19] Jun Li, Guiqiong Jiao, Bo Wang, Liang Li, and Chengpeng Yang. Damage characteristics and constitutive modeling of the 2d c/sic composite: Part ii–material model and numerical implementation. *Chinese Journal of Aeronautics*, 28(1):314–326, 2015.

[20] Jean-Louis Chaboche. Continuum damage mechanics: Part igeneral concepts. *Journal of applied mechanics*, 55(1):59–64, 1988.

[21] F Laurin, N Tableau, M Kaminski, Z Aboura, and Florence Bouillon. Validation of the onera damage model through comparisons with multi-instrumented structural tests on interlock woven ceramic matrix composites. In *16th European Conference on Composite Materials*, 2014.

[22] JL Chaboche, PM Lesne, and JF Maire. Macroscopic modelling and damage processes in cmc's. *Ceram. Trans. Vol. 57*, pages 65–75, 1995.

[23] ALJTR Matzenmiller, J Lubliner, and RL Taylor. A constitutive model for anisotropic damage in fiber-composites. *Mechanics of materials*, 20(2):125–152, 1995.

[24] Xavier Aubard, Jacques Lamon, and Olivier Allix. Model of the nonlinear mechanical behavior of 2d sic–sic chemical vapor infiltration composites. *Journal of the American Ceramic Society*, 77(8):2118–2126, 1994.

[25] Yutai Katoh, Lance Lewis Snead, Charles H Henager Jr, Akira Hasegawa, Akira Kohyama, Bruno Riccardi, and Hans Hegeman. Current status and critical issues for development of sic composites for fusion applications. *Journal of Nuclear Materials*, 367:659–671, 2007.

[26] Yukiya Amano. The fukushima daiichi accident: Report by the director general. *International Atomic Energy Agency, Vienna, Austria, Report No. GC (59)/14. http://www-pub. iaea. org/MTCD/Publications/PDF/Pub1710-ReportByTheDG-Web. pdf*, 2015.